

# Flattening of the Lung Surface with Temporal Consistency for the Follow-Up Assessment of Pleural Mesothelioma

Peter Faltin<sup>1</sup>, Thomas Kraus<sup>2</sup>, Marcin Kopaczka<sup>1</sup> and Dorit Merhof<sup>1</sup>

<sup>1</sup>*Institute of Imaging and Computer Vision, RWTH Aachen University, Aachen, Germany*

<sup>2</sup>*Institute and Out-patient Clinic of Occupational Medicine, Uniklinik RWTH Aachen, Aachen, Germany*

**Keywords:** Surface Representation, Planar Visualization, Multidimensional Scaling, Flattening, Temporal Consistency.

**Abstract:** Malignant pleural mesothelioma is an aggressive tumor of the lung surrounding membrane. The standardized workflow for the assessment comprises an inspection of 3D CT images to detect pleural thickenings which act as indicators for this tumor. Up to now, the visualization of relevant information from the pleura has only been superficially addressed. Current approaches still utilize a slice-wise visualization which does not allow a global assessment of the lung surface. In this publication, we present an approach which enables a planar 2D visualization of the pleura by flattening its surface. A distortion free mapping to a planar representation is generally not possible. The present method determines a planar representation with low distortions directly from a voxel-based surface. For a meaningful follow-up assessment, the consistent representation of a lung from different points in time is highly important. Therefore, the main focus in this publication is to guarantee a consistent representation of the pleura from the same patient extracted from images taken at two different points in time. This temporal consistency is achieved by our newly proposed link of both surfaces during the flattening process. Additionally, a new initialization method which utilizes a flattened lung prototype speeds up the flattening process.

## 1 INTRODUCTION

Asbestos is a silicate mineral which was commonly used in many countries because of its advantageous properties, e.g. resistance to acid and heat. During mechanical processing, asbestos fibers can get into the lung by inhalation. A deposition of these fibers in the tissue can cause different kinds of cancer such as the malignant pleural mesothelioma (MPM) which is an aggressive tumor of the pleura. The pleura is a lung surrounding membrane consisting of two layers. Because of the long latency of about 38 years and a peak usage of asbestos in the 1980s, an increasing number of MPM cases is expected in Europe till 2018 (Pistolesi and Rusthoven, 2004). In some other countries, especially in Asia, the asbestos consumption is still rising (Virta, 2012). Therefore, an increasing number of MPM cases is expected in these countries. Because of the aggressive tumor growth, early stage detection is absolutely essential. For this purpose, high risk patients undergo a regular medical check-up. These checks also include CT image acquisition to identify pleural thickenings which are indicators for the MPM. Especially the identification of their growth is an im-



Figure 1: CT slice with thickenings indicated by orange circles.

portant aspect in the diagnosis. The growth can be estimated by a follow-up assessment, based on images from two different points in time.

As shown in Figure 1, pleural thickenings are difficult to spot because of the low image contrast between their tissue and the surrounding tissue. At an early stage, they have a small thick-

ness in terms of the image resolution of typically 1-3 voxels. Therefore, a manual analysis of the images is time consuming and subject to strong inter- and intra-reader variability (Ochsmann et al., 2010). Several (semi-)automated methods (Rudrapatna et al., 2005; Chen et al., 2011; Frauenfelder et al., 2011; Sensakovic et al., 2011; Faltin et al., 2013; Kengne Nzegne et al., 2013) have been developed to support the physician in the decision process. Nevertheless, the final decision is made by the physician. For this purpose, a visualization of the relevant data is highly important. Two publications (Faltin et al., 2013; Kengne Nzegne et al., 2013) propose a global 3D visualization of the thickening locations, while other publications only consider 2D slice-wise visualization. With the 3D visualization a global overview is possible. However, due to the 3D shaped surface, thickenings might be occluded and the affected areas on the surface can only be qualitatively recognized. A slice-wise view facilitates a more precise assessment of the affected surface, but it is time consuming, does not visualize the complex thickening morphologies, and does not give an overview. To address these issues, a planar visualization of the lung surface is suggested in this publication. An exemplary mapping of a 3D lung surface into a planar visualization is shown in Figure 2. This kind of visualization enables a global overview and a precise recognition of the affected areas on the surface. Different features, e.g. tissue attenuation or surface roughness are utilized in a manual or automated thickening identification. These features can be visualized for the whole lung at once by utilizing the planar representation. Beside the detection of thickenings, it is important to compare the different points in time for a growth assessment. For this purpose the planar representations of the lung at both points in time need to be consistent regarding their spatial arrangement.

The concept of mapping a 2D surface from a 3D space to a planar 2D space is often referred to as flattening. To provide a meaningful interpretation of the flattened surface, the mapping should preserve angles and be equiareal, as far as possible. If both angle and area are preserved the mapping is called isometric or distance-preserving. However, an isometric mapping of arbitrary shaped surfaces is not generally possible (Floater and Hormann, 2005). The aim of flattening methods is to approximate this isometric mapping. Most of these methods (Zigelman et al., 2002; Bronstein et al., 2003; Tosun et al., 2004; Zhao et al., 2013; Hurdal and Stephenson, 2009) are based on triangular meshes. In our case, the relevant feature information is available for each of the 350 000 lung surface voxels. For a mesh-based flat-

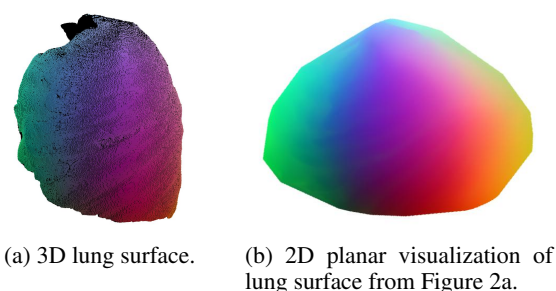


Figure 2: Exemplary mapping of the 3D surface to a planar 2D visualization. The 3D coordinates of each surface point are taken as color components for a RGB coding.

tening a very highly resolved mesh needs to be processed or resampled. This results either in high computational demands or the need of additional mesh simplification methods which might induce inaccuracies. An efficient alternative is the method from Saroul et al. (Saroul et al., 2006) which can be directly applied on discrete voxel data and focuses on an interactive visualization with adjustable planes and a center of low distortion. However, it does not include a global optimization of the chosen plane. Therefore, our approach utilizes multidimensional scaling (MDS) which has been applied for the flattening of discrete surfaces (Grossmann et al., 2002) and provides a global optimization on a discrete voxel surface. With this approach, the preserved surface distances are directly calculated on the high resolution data set and the computation can still be performed on a down-sampled set of surface points. In this publication, we suggest a new method to link both points in time globally to achieve consistent representations of the surfaces. Existing approaches to compare similar shaped surface (Tosun et al., 2004; Zhao et al., 2013; Hurdal and Stephenson, 2009) often use a standardized mapping target. The approach from Bronstein et al. (Bronstein et al., 2003) was especially designed for an inter- and intra-subject comparison. However, none of these approaches uses a mapping target which is individually optimized for each subject. In contrast to these methods, our method results in subject adapted representations and facilitates the comparison between different points in time. Additionally, we deduce a method to efficiently initialize the MDS process to speed up the processing of a similar shaped surface. For this purpose, the results of a flattening from a prototype lung are utilized. A closed-form solution to directly compute the initial points from this prototype is derived.

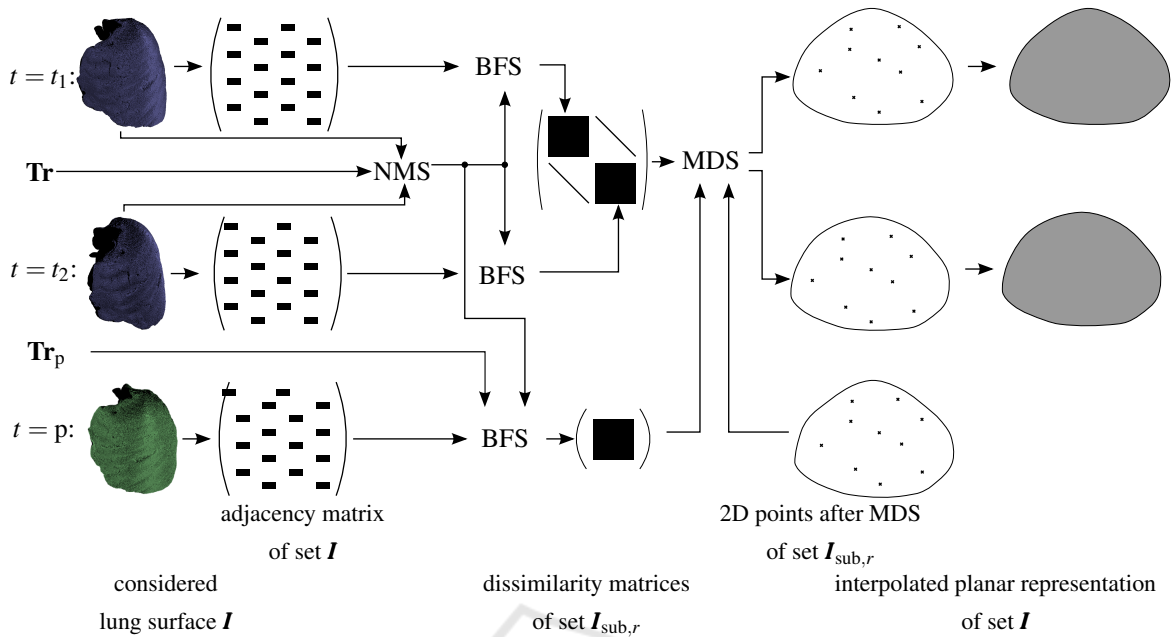


Figure 3: Overview of the presented method: First, an adjacency matrix is extracted from the lung surface of the two points in time  $t_1$  and  $t_2$  and the prototype surface  $t = p$ . By a non-maxima suppression (NMS) the set  $I$  of all surface points is reduced to the set  $I_{sub,r} \subset I$ . From the full adjacency matrices and the reduced point set, the dissimilarities are extracted by a breadth first search (BFS). Then, the multidimensional scaling (MDS) extracts a subsampled 2D representation. Finally, an interpolation by radial basis functions (RBF) is used to determine a full planar visualization. The prototype  $t = p$  can be used to initialize the MDS. To connect the different lung surfaces, the transformations  $Tr$  and  $Tr_p$  are required.

## 2 METHODS

In the first part of this section, the extraction of the discrete lung surface is shortly described. This is followed by a general introduction to MDS. The idea of mapping a discrete 3D surface to a 2D plane by MDS was introduced by Grossmann et al. (Grossmann et al., 2002) and is described in Section 2.3, 2.4 and 2.6. We embed this method into a follow-up assessment which requires a temporal consistent flattening at both points in time. This methodical extension is described in Section 2.5. To speed up the flattening processing, we also derive an initialization approach to map the data from a flattened prototype lung to an actual lung, described in Section 2.7. An overview of the complete work flow is shown in Figure 3.

### 2.1 Discrete Lung Surface

The extraction of the discrete lung surface  $\partial R$  from the chest CT image data  $g$  is performed in multiple steps, as shown in Figure 4. Firstly, the body is segmented by a simple thresholding, keeping the largest connected component, followed by a morphological filling. The chosen threshold of -250 HU is not critical regarding the exact value. Within this body segment,

the lungs are identified. In this case the exact threshold of -250 HU is relevant and conforms to the lower boundary of the standard thickening window. This window is used to visualize the CT data  $g$  in a standardized manual assessment of pleural thickenings. Additionally, the mediastinal region  $R_{medias}$  in between left and right lung is identified. It is the largest concave region of the lung surfaces in each slice. Finally, a discrete surface which guarantees connectivity within a 26-connected neighborhood  $\mathcal{N}_{26}$  is extracted. For this purpose, a lung mask with removed 6-neighborhood  $\mathcal{N}_6$  is subtracted from the segmented lung  $R$  itself

$$\partial R_{full} = R \setminus (R \ominus \mathcal{N}_6), \quad (1)$$

with the morphological erosion  $\ominus$ . The surface part surrounded from the mediastinal region  $R_{medias}$  is excluded, because it is not relevant for the thickening assessment. The resulting lung surface is given by

$$\partial R = \partial R_{full} \setminus (R_{medias} \oplus \mathcal{N}_{26}), \quad (2)$$

with the morphological dilation  $\oplus$ .

### 2.2 Multidimensional Scaling

MDS is an approach to map a set of  $N$  points into a space of any dimension  $M$ , by considering only

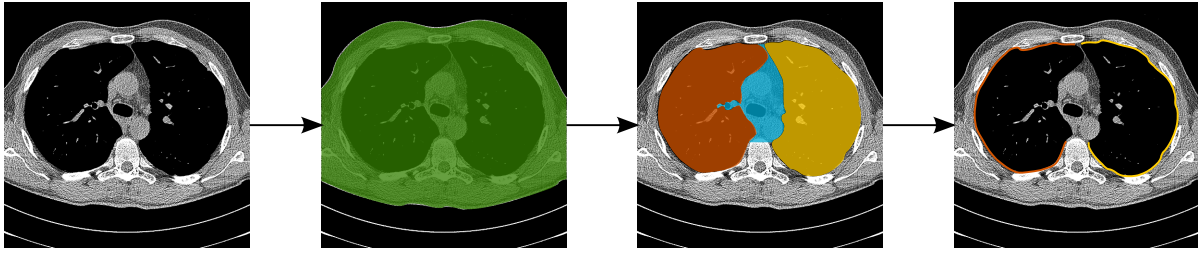


Figure 4: 2D visualization of the lung surface segmentation for an exemplary slice. First, the body (green) is detected, then lungs (yellow and orange) and mediastinum (blue) are segmented. Finally, the pleura surface is extracted (yellow and orange).

the dissimilarities  $\delta_{i,j}$  of the data points, with  $i, j \in \mathbf{I} = \{1 \dots N\}$ . This section gives a short idea of the method. Details can be found in the relevant literature (Cox and Cox, 2001). The results are only meaningful if the dissimilarities can be, at least approximately, described in the target space of dimension  $M$ . In the target space, the positions  $\mathbf{p}_{MD,i}$  are estimated depending on their distances  $d_{i,j} = \|\mathbf{p}_{MD,i} - \mathbf{p}_{MD,j}\|$ . These distances should be as close as possible to the associated dissimilarities in the original space. This is achieved by solving

$$\partial \mathbf{R}_{MD} = \arg \min_{\mathbf{p}_{MD,1}, \dots, \mathbf{p}_{MD,N}} \text{loss}_{\Delta}(\mathbf{p}_{MD,1}, \dots, \mathbf{p}_{MD,N}), \quad (3)$$

with a certain loss measure and the matrix  $\Delta$  containing the dissimilarities  $\delta_{i,j}$ . The MDS methods in literature are differentiated into

- classical vs. non-classical and
- metric vs. non-metric

approaches. These terms and the resulting loss criteria named stress or strain are sometimes ambiguously used. In this publication the terminology from Buja et al. (Buja et al., 2008) is chosen and non-classical MDS with the loss criterion

$$\begin{aligned} & \text{loss}_{\Delta}(\mathbf{p}_{MD,1}, \dots, \mathbf{p}_{MD,N}) \\ &= \text{Sstress}_{\Delta}(\mathbf{p}_{MD,1}, \dots, \mathbf{p}_{MD,N}) \\ &= \frac{\sum_{\substack{i,j=1 \dots N \\ i \neq j}} (d_{i,j}^2 - \delta_{i,j}^2)^2}{\sum_{\substack{i,j=1 \dots N \\ i \neq j}} (\delta_{i,j}^4)} \end{aligned} \quad (4)$$

is utilized. This criterion is differentiable even if two points are coincident. The solution is found by a gradient-based minimization, utilizing the conjugate-gradient method (Navon and Legler, 1987). Weighting terms  $w_{i,j}$  for each pair of points can be chosen

individually, resulting in the new criterion

$$\begin{aligned} & \text{Sstress}_{\Delta, \mathbf{W}}(\mathbf{p}_{MD,1}, \dots, \mathbf{p}_{MD,N}) \\ &= \frac{\sum_{\substack{i,j=1 \dots N \\ i \neq j}} w_{i,j} (d_{i,j}^2 - \delta_{i,j}^2)^2}{\sum_{\substack{i,j=1 \dots N \\ i \neq j}} (w_{i,j} \delta_{i,j}^4)}, \end{aligned} \quad (5)$$

with the weights denoted by the matrix  $\mathbf{W}$  of same size as  $\Delta$ . In the case of a planar visualization, the target dimension is chosen as  $M = 2$ .

### 2.3 Distances on Discrete Surface

As described in the last section, the optimization for the 2D representation aims for distances  $d_{i,j}$  identical to the dissimilarities  $\delta_{i,j}$ . For a surface flattening, the dissimilarities are chosen as the distances on the lung surface between all surface points  $\mathbf{p}_{3D} \in \partial \mathbf{R}$  (Grossmann et al., 2002). To calculate the distances between the discrete points on the surface, first a weighted adjacency matrix with distances between the connected surface points  $\mathbf{p}_{3D,i}$  with  $i \in \mathbf{I}$ ,  $\mathbf{I} = \{1 \dots |\partial \mathbf{R}|\}$  of a 26-connected neighborhood is extracted. Based on this information, a breadth first search (BFS), based on the Boost C++ Library (Gleich, 2009), is used to determine the distances on the surface. A lung surface has approximately  $|\partial \mathbf{R}| = 350\,000$  surface points. Just to store all pair distances, approximately 450 GB of memory would be necessary. So, the distances are only extracted for a subsampled number of surface points. A regular subsampling of the unparameterized 3D surface is not easily possible. Therefore, non-maxima suppression (Neubeck and Gool, 2006) (NMS) with a suppression radius  $r$  is applied to the binary surface  $\partial \mathbf{R}$ . The free parameter  $r$  represents a compromise between exact surface description and computational complexity. In this case, the NMS on a binary image is only utilized to generate a uniformly distributed subset of points  $\partial \mathbf{R}_{\text{sub},r} \subset \partial \mathbf{R}$ , with

$$\|\mathbf{p}_{3D,i} - \mathbf{p}_{3D,j}\| \geq r, \forall i, j \in \mathbf{I}, i \neq j. \quad (6)$$

The indices of the subsampled surface points are contained in the set  $\mathbf{I}_{\text{sub},r} \subset \mathbf{I}$ . Also other point distribu-

tion algorithms could be applied. The NMS was chosen to be conforming to the procedure in a subsequent step.

## 2.4 Surface Mapping for a Single Point in Time

The sample points describe a 2D surface embedded in a 3D space, therefore a meaningful 2D representation can be obtained, but of course a perfect isometric mapping cannot be achieved. All sample points are mapped depending on their dissimilarities  $\delta_{i,j} = \delta(\mathbf{p}_{3D,i}, \mathbf{p}'_{3D,j})$ ,  $\forall i, j \in \mathbf{I}_{\text{sub},r}$  and independent on their actual 3D position  $\mathbf{p}_{3D,i}$ . These dissimilarity measures  $\delta_{i,j}$  are given by the surface distances from Section 2.3. Solving the minimization problem in Equation 3 leads to the 2D representation  $\partial\mathbf{R}_{2D}$ . This representation is not unique regarding the degrees of freedom (DOF) rotation, translation and reflection, as these properties are not observable from the dissimilarities. For a single surface all weights  $w_{i,j}$  are kept equal to one, if all regions are of similar importance. Focusing on some important regions which are, e.g. subject to thickenings can be achieved by increasing the weights in these regions.

## 2.5 Consistent Mapping for Two Points in Time

The process described in the previous section, could be independently applied to the lungs' surfaces of the same patient from images, taken at two different points in time. In most cases, this leads, beside the DOFs, to a similar spatial arrangement of the points in 2D which is however not guaranteed. The problem described in Equation 3 might have multiple solutions and also local minima. To avoid different solutions at both points in time, we propose to join both independent problems into a single problem. For this purpose, identical points on the lung surfaces  $\partial\mathbf{R}_{t_1}$  and  $\partial\mathbf{R}_{t_2}$  from both points in time  $t_1$  and  $t_2$  are linked by enforcing identical target positions in the 2D visualization.

Firstly, suitable points to establish a link are selected. They should be located at the same 3D surface position for both points in time, after a registration  $\mathbf{Tr} : \mathbf{p}_{3D,t_1,i} \mapsto \mathbf{p}_{3D,t_2,i'}$ . This registration is usually not perfect and afterwards the points  $\mathbf{Tr}(\mathbf{p}_{3D,t_1,i})$  and  $\mathbf{p}_{3D,t_2,i'}$  are not identical. For each surface point  $\mathbf{p}_{3D,t_1,i}$ ,  $i \in \mathbf{I}$  the closest point at the other point in time and their temporal distance is extracted by utilizing the  $k$ -d tree algorithm (Bentley, 1975).

$$\text{conn}(i) = \arg \min_{i'=1 \dots |\partial\mathbf{R}_{t_2}|} \|\mathbf{Tr}(\mathbf{p}_{3D,t_1,i}) - \mathbf{p}_{3D,t_2,i'}\|_2 \quad (7)$$

$$d_t(i) = \mathbf{p}_{3D,t_1,i} - \mathbf{p}_{3D,t_2,\text{conn}(i)}, \quad (8)$$

In the subsampling process, point pairs which can be well aligned by the registration should be locally preferred to pairs which can only be poorly aligned by the registration. This quality can be measured by the temporal distance  $d_t(i)$ . Therefore, the NMS (Neubeck and Gool, 2006) with radius of  $r$  is now applied to the inverse distances  $\frac{1}{d_t(i)}$  to obtain the subsampled set  $\mathbf{I}_{\text{sub},r}$  for the linking process. The flattening in regions of high importance could be improved by keeping additional points in these regions. Points within growing thickening regions will result in inconsistent surface distances at both points in time and should be avoided. Strong growth also results in large temporal distances. Hence, thickening points which are critical for the flattening are suppressed automatically.

In the second step, the minimization problems are independently formulated as in the previous section and then connected. The set of linked points does not have to be identical with the set of subsampled points in Section 2.3. However, the problem statement is given by the matrices  $\mathbf{W}$  and  $\mathbf{\Delta}$ , whose size depends on the number of involved points. Therefore, the point sets are chosen to be identical to reduce the number of variables in the optimization problem. The matrices  $\mathbf{\Delta}_{t_1}$  and  $\mathbf{\Delta}_{t_2}$  are the dissimilarities for the different points with identical order of the points at both points in time. So, the entries  $\delta_{t_1,i,j}$ ,  $\delta_{t_2,\text{conn}(i),\text{conn}(j)}$  correspond to the same point combination at both points in time, because point  $i$  corresponds to point  $i'$  and  $j$  corresponds to  $j'$ . Then, the matrices describing the linked problem are

$$\mathbf{\Delta}_{\text{conn}} = \begin{pmatrix} \mathbf{\Delta}_{t_1} & \mathbf{0} \\ \mathbf{0} & \mathbf{\Delta}_{t_2} \end{pmatrix}, \quad (9)$$

$$\mathbf{W}_{\text{conn}} = \begin{pmatrix} \mathbf{1} & \kappa \text{diag}(1, \dots, 1) \\ \kappa \text{diag}(1, \dots, 1) & \mathbf{1} \end{pmatrix}, \quad (10)$$

with  $\mathbf{1}$  being matrices of size  $|\mathbf{I}_{\text{sub},r}| \times |\mathbf{I}_{\text{sub},r}|$  with ones in each entry,  $\text{diag}(1, \dots, 1)$  being matrices of same size with ones on the diagonal and zeros at each other entry, and  $\mathbf{0}$  being a matrix of same size with zeros at each entry. The parameter  $\kappa$  is a free weighting parameter to balance the influence of inter- and intra-temporal distances given in  $\mathbf{\Delta}_{\text{conn}}$ . Only the diagonal entries of the matrices  $\mathbf{0}$  are relevant to set the temporal distances of connected points. The other entries are of no importance and are ignored because of their zero weights in  $\mathbf{W}_{\text{conn}}$ . Finally, the connected problem can be solved as described in Equation 3.

## 2.6 Interpolation

Only the subset of points  $\mathbf{I}_{\text{sub},r}$  is mapped to points  $\mathbf{p}_{2D,c}$ ,  $c \in \mathbf{I}_{\text{sub},r}$  on the 2D plane by MDS. For all other discrete image points  $\mathbf{p}_{3D,i}$ ,  $i \in (\mathbf{I} \setminus \mathbf{I}_{\text{sub},r})$  their matching 2D positions  $\mathbf{p}_{2D,i}$  are estimated by an interpolation based on radial basis functions (RBF) (Morse et al., 2005). RBF approximate a function  $f$  by a sum of radially symmetric functions  $\Phi$ , around the subsampled points  $\mathbf{p}_{3D,c}$  with  $c \in \mathbf{I}_{\text{sub},r}$  by

$$f_{\zeta}(\mathbf{p}_{3D,i}) = \text{poly}_{\zeta}(\mathbf{p}_{3D,i}) + \sum_{c \in \mathbf{I}_{\text{sub},r}} \lambda_{\zeta}(c) \Phi(\|\mathbf{p}_{3D} - \mathbf{p}_{3D,c}\|), \quad (11)$$

for any point  $\mathbf{p}_{3D,i}$ , where  $\lambda_{\zeta}(c)$  are individual weighting terms for each center point  $\mathbf{p}_{3D,c}$ ,  $\text{poly}_{\zeta}(\mathbf{p}_{3D,i})$  represents the polynomial part of the function, and  $\zeta$  allows the separate interpolation for both planar dimensions  $\zeta \in \{x, y\}$ . A resulting planar point  $\mathbf{p}_{2D,i}$  is given by  $\mathbf{p}_{2D,i} = (f_x(\mathbf{p}_{3D,i}), f_y(\mathbf{p}_{3D,i}))^T$ . The weights  $\lambda_{\zeta}(c)$  and coefficients for the polynomial part  $\text{poly}_{\zeta}$  are determined by a least squares approach (Morse et al., 2005), considering all mapped points  $\mathbf{I}_{\text{sub},r}$ . This method has been successfully applied to various medical interpolation problems (Carr et al., 1997; Morse et al., 2005). Different RBFs with similar interpolation results have been applied in preliminary experiments. In this publication, only radially symmetric function  $\Phi(\rho) = \rho$  is regarded in detail which showed a slightly superior performance.

## 2.7 Initialization

MDS is an optimization process, thus its calculation time depends on the initialization with the 2D point positions. To reduce the calculation time a prototype lung can be utilized. For this prototype, a planar representation must be calculated once. Then, it can be utilized for all future flattening processes. A registration  $\mathbf{Tr}_p: \mathbf{p}_{3D,i} \mapsto \mathbf{p}_{3D,p,i}$  between points  $\mathbf{p}_{3D,p,i} \in \partial \mathbf{R}_p$  of the prototype lung surface and the corresponding points  $\mathbf{p}_i \in \partial \mathbf{R}$  of the actual lung surface  $\partial \mathbf{R}$  is required. For the subsampled points with indices  $i \in \mathbf{I}_{\text{sub},r}$ , the initial 2D positions can be approximated from the prototype positions  $\mathbf{p}_{2D,p,i}$ .

Different physical dimensions of the actual and prototype lung in 3D cannot be directly transferred to the planar 2D representation. The 2D offset between two points is a mixture of the 3D offset, obtained from the optimization process. However, we deduce an approximation for a deformation of the flattened prototype which considers different 3D dimensions of the lung. As a result of Section 2.3, the surface distance between two points  $\mathbf{p}_i$  and  $\mathbf{p}_j$  is calculated by a sum

of distances between neighboring surface points, on the shortest path  $\mathbf{E}$  between those points. This path is described by the edges  $(\mu, \nu)^T \in \mathbf{E}$  and results in the surface distance

$$\delta_{i,j} = \sum_{(\mu,\nu)^T \in \mathbf{E}} \|\mathbf{p}_{3D,\mu} - \mathbf{p}_{3D,\nu}\|. \quad (12)$$

An isometric mapping to 2D is not possible for lung surfaces and therefore, the distances between the points  $\mathbf{p}_{2D,\mu}$  and  $\mathbf{p}_{2D,\nu}$  of each edge  $(\mu, \nu)^T$  are subject to an error caused by the mapping. The planar distances can therefore be described by

$$d_{i,j} = \sum_{(\mu,\nu)^T \in \mathbf{E}} e_{\mu,\nu} \underbrace{\|\mathbf{p}_{3D,\mu} - \mathbf{p}_{3D,\nu}\|}_{\delta_{\mu,\nu}}, \quad (13)$$

with the mapping error  $e_{\mu,\nu}$ . The prototype and actual lungs have similar shapes and the aim is a similar 2D mapping. Therefore, it is assumed that the distance  $d_{p,i,j}$ , of the corresponding points  $\mathbf{p}_{2D,p,i}$  and  $\mathbf{p}_{2D,p,j}$  on the prototype surface, is subject to the same mapping errors  $e_{\mu,\nu}$  and given by the same shortest path  $\mathbf{E}$ . Then, the prototype distance of two neighbor points is given by

$$d_{p,\mu,\nu} = e_{\mu,\nu} \underbrace{\|\mathbf{Tr}_p(\mathbf{p}_{3D,\mu}) - \mathbf{Tr}_p(\mathbf{p}_{3D,\nu})\|}_{\delta'_{\mu,\nu}}. \quad (14)$$

As a result of Equation 13 and 14, the planar distances of the actual lung can be approximated by

$$d_{i,j} = \sum_{(\mu,\nu)^T \in \mathbf{E}} \frac{\delta_{\mu,\nu}}{\delta'_{\mu,\nu}} d_{p,\mu,\nu}, \quad (15)$$

with the planar distances  $d_{p,\mu,\nu}$  known from the prototype and the shortest path  $\mathbf{E}$ , which can be efficiently calculated during the BFS (Gleich, 2009), discussed in Section 2.3.

By choosing a fixed point  $\mathbf{p}_{2D,f}$ , with  $f \in \mathbf{I}_{\text{sub}}$ , the distances  $d_{f,i}$  from Equation 15 to this point can be used for an initialization. The position  $\mathbf{p}_{2D,i}$  of all other points  $i \in \mathbf{I}_{\text{sub}} \setminus \{f\}$  can be described in polar coordinates, as shown in Figure 5, by

$$\mathbf{p}_{2D,i} = \mathbf{p}_{2D,f} + d_{f,i} \begin{pmatrix} \cos(\phi_{f,i}) \\ \sin(\phi_{f,i}) \end{pmatrix}, \quad (16)$$

and for the prototype by

$$\mathbf{p}_{2D,p,i} = \mathbf{p}_{2D,p,f} + d_{p,f,i} \begin{pmatrix} \cos(\phi_{p,f,i}) \\ \sin(\phi_{p,f,i}) \end{pmatrix}, \quad (17)$$

with the unknown angles  $\phi_{f,i}$  and  $\phi_{p,f,i}$ . Without loss of generality these angles and also the fixed point can be chosen identically

- $\mathbf{p}_{2D,f} = \mathbf{p}_{2D,p,f}$  results in identical translation, and

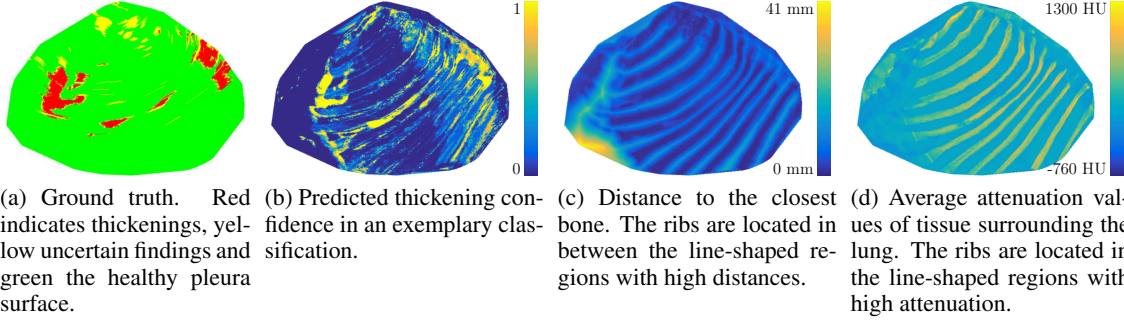


Figure 6: Planar visualization of lung surface with ground truth of thickening locations, automatic prediction, and exemplary features considered for the prediction.

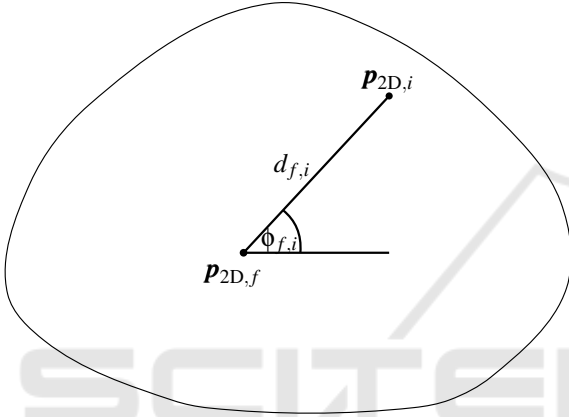


Figure 5: Sketch of the planar lung surface, with description of the point  $\mathbf{p}_{2D,i}$ , relative to the fixed point  $\mathbf{p}_{2D,f}$  in polar coordinates  $d_{f,i}$  and  $\phi_{f,i}$ .

- $\phi_{f,i} = \phi_{p,f,i}$  results in identical rotation and reflection

of prototype and actual lung. Finally, the initial point position is approximated by

$$\mathbf{p}_{2D,i} = \mathbf{p}_{2D,p,f} + \frac{d_{f,i}}{d_{p,f,i}} (\mathbf{p}_{2D,p,i} - \mathbf{p}_{2D,p,f}). \quad (18)$$

The derived initialization does not compensate potential changes in the angle  $\phi_{f,i}$ , caused by the different spacings. Therefore, they are subject to a mapping error  $\phi_{err,f,i}$  and the correct condition is

$$\phi_{f,i} = \phi_{p,f,i} + \phi_{err,f,i}, \quad (19)$$

resulting in the point positions  $\tilde{\mathbf{p}}_{2D,i}$ . So the error caused by incorrect angles is

$$\varepsilon_i = \|\mathbf{p}_{2D,i} - \tilde{\mathbf{p}}_{2D,i}\|^2. \quad (20)$$

With the help of trigonometric functions and Equations 16 and 20 it can be shown, that the error is

$$\varepsilon_i = 2d_{f,i}^2 \sin^2\left(\frac{\phi_{err,f,i}}{2}\right). \quad (21)$$

Since the term  $\sin^2\left(\frac{\phi_{err,f,i}}{2}\right)$  cannot be determined without the solution, it is replaced by an unknown expected value which is assumed to be identical for all combinations of  $f$  and  $i$ . Under this condition, the fixed point, which minimizes the overall error  $\sum_i \varepsilon_i$ , is given by the mean value of all points

$$\mathbf{p}_{2D,opt,f} = |\mathbf{I}_{sub}|^{-1} \sum_{i=1}^{|\mathbf{I}_{sub}|} \mathbf{p}_{2D,i}. \quad (22)$$

A prototype lung should have a similar shape to the processed lung so the surfaces can be well aligned by the registration  $\mathbf{Tr}_p$ . That is why creating a mean shape as a prototype could improve the initialization. If the prototype and actual lung are too different, the assumptions in this section might not hold. However, the resulting imperfect initialization would not have a negative influence on the mapping quality, but only on the computation time.

### 3 RESULTS

To assess potential thickenings at an early stage, high resolution chest CT data with a resolution of  $512 \times 512 \times 600$  to  $512 \times 512 \times 700$  voxels is utilized. The anisotropic image resolution varies between 0.63 mm and 1 mm in the transverse plane and between 0.5 mm and 0.8 mm orthogonal to this plane. Altogether, twenty data sets from ten different patients at two different points in time have been evaluated. All calculations have been performed on an Intel Core i5 with 16 GB of memory.

Some visual results for an exemplary patient are given in Figure 6. The ground truth, extracted on the volumetric data from a physician by labeling approximately 550 2D slices, is shown in the first image 6a. The following images 6c–6d show relevant scalar features which have been extracted on the lung surface for each surface point and Figure 6b shows the confidence of an exemplary thickening classification, not

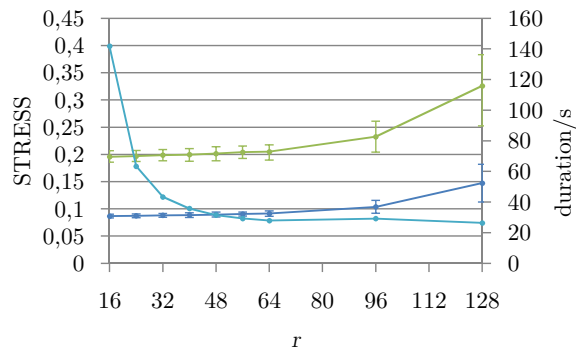
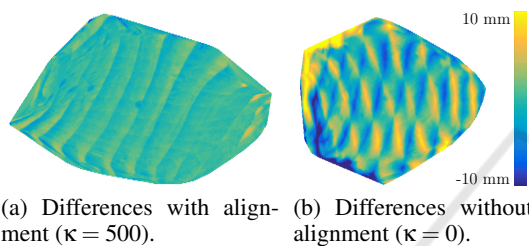


Figure 7: Distortion and computation time, depending on radius  $r$  for the non-maxima suppression. The results are given as mean values for all patients of left and right lung. The error bars indicate the standard deviation.



(a) Differences with alignment ( $\kappa = 500$ ). (b) Differences without alignment ( $\kappa = 0$ ).

Figure 8: Planar visualization of a lung at two points in time from the same patient. The colors represent the differences of the rib distances clipped to the interval  $[-10, 10]$  mm.

discussed in this publication. For a quantitative assessment, the duration and the error of the flattening as stress (Kruskal, 1964)

$$\text{STRESS1} = \left( \frac{\sum_{i,j \in \mathcal{I}} (d_{i,j} - \delta_{i,j})^2}{\sum_{i,j \in \mathcal{I}} \delta_{i,j}^2} \right)^{0.5}, \quad (23)$$

$$\text{STRESS2} = \left( \frac{\sum_{i,j \in \mathcal{I}} (d_{i,j} - \delta_{i,j})^2}{\sum_{i,j \in \mathcal{I}} (d_{i,j} - \text{mean}(d_{i,j}))^2} \right)^{0.5} \quad (24)$$

is plotted against the radius  $r$  of the NMS. The stress measures indicate if the distances  $\delta_{i,j}$  on the 3D surface are similar to the distances  $d_{i,j}$  in the planar representation. Low stress indicates similar distances and high stress different distances. A vague verbal scale of the STRESS1 measures was published by Kruskal (Kruskal, 1964): starting with a values of 0 for perfect matching and ending with a value of 0.2 for poor matching. The average results for the left and right lung of 10 patients at one point in time are given in Figure 7.

For the temporal consistent flattening, a non-rigid registration, based on B-splines (Rueckert et al., 1999), was applied. This registration has already been

utilized for the automated assessment of the thickenings and is available at no extra computational cost. An exemplary visual comparison of two points in time showing the effect of temporal consistency is shown in Figure 8. The relation of slice-wise visualization and planar visualization for a growing thickening is shown in Figure 11. Quantitative results for the consistent planar visualization are given in Figure 9. The radii values (visualized by the different colors), leading to stable results for the planar visualization of a single point in time with different connection strengths  $\kappa \in \{0, 1, 500, 1000\}$  (indicated by the grouping). Additionally to the average STRESS1 criterion, shown in Figure 9a, the average temporal distance between both data sets on the 2D plane

$$\bar{d}_{2D} = \frac{1}{|\partial \mathbf{R}_{t_1}|} \sum_{i=1 \dots |\partial \mathbf{R}_{t_1}|} \min_{i'=1 \dots |\partial \mathbf{R}_{t_2}|} d_{2D}(\mathbf{p}_{2D,t_1,i}, \mathbf{p}_{2D,t_2,i'}) \quad (25)$$

with

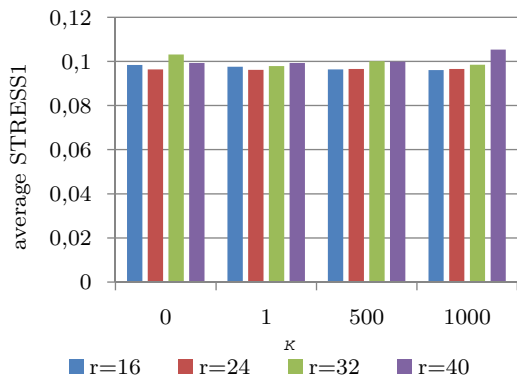
$$d_{2D}(\mathbf{p}_i, \mathbf{p}_j) = \|\mathbf{p}_{2D,t_1,i} - \mathbf{p}_{2D,t_2,j}\|_2 \quad (26)$$

is given in Figure 9b to evaluate the consistency.

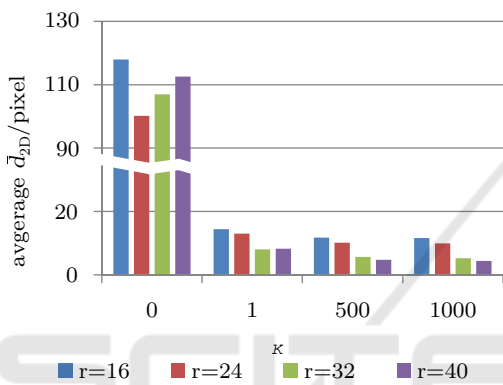
For the MDS initialization, a rough mapping to the prototype is sufficient. Therefore, only a simple rigid registration was applied which can be calculated in a couple of seconds, while a non-rigid registration takes typically a couple of minutes (Glocker et al., 2010). An additional lung, not utilized in the evaluation, has been chosen as the prototype. The calculation time for the different components: adjacency matrix, dissimilarity calculation by BFS and the MDS (with and without initialization) are given in Figure 10. The duration of the initialized MDS covers all additional computations required, namely, the mapping of the points  $\text{Tr} : \mathbf{p}_{3D,i} \mapsto \mathbf{p}_{3D,p,i}$  and the initialization itself.

## 4 DISCUSSION

Comparing the resulting computation time and the quality of the flattening process depending on the radius, as shown in Figure 7, reveals a good compromise of calculation time and error for  $r = 40$ . On average, the smallest evaluated radius of  $r = 16$  results in approximately 2350 surface points, the radius  $r = 40$  results in approx. 410 surface points and a radius of  $r = 128$  results in only 14 surface points. For smaller radii the computation time is significantly larger and for larger radii the computation time is only slightly decreasing, while the error is strongly increasing. The stress stays relatively low even for large radii, which indicates a good performance of the RBFs in interpolating the lung shape. The relatively large acceptable



(a) The average STRESS1 results.



(b) The average distances between the 2D representations of both points in time.

Figure 9: Results for consistent mapping for various radii  $r$  and various weights  $\kappa$ .

radius of  $r = 40$  might be surprising at first glance. However the experiments showed that it is important to map a few point optimally to the planar plane, and all points in between can be interpolated with a similar quality as the mapping itself. An analogy would be to thinly cover a 3D surface with liquid rubber. After cooling down, the resulting rubber sheet can be pinned to a planar surface at a few fixed points. If the fixed points are chosen properly, the rubber sheet arranges the surface in between these points automatically with low stress. The stress asymptotically approaches a minimum value larger zero, which is caused by the shape of the lung itself which does not allow a perfect isometric mapping.

As shown in Figure 9b, the temporal distance between two points in time is significantly reduced for  $\kappa = 1$ , but decreases only slightly for larger values  $\kappa \in \{500, 1000\}$ . As expected, both points in time can be represented by a similar planar representation. Therefore, the problem defined by the matrices in Equations 9 and 10 need only a small connection

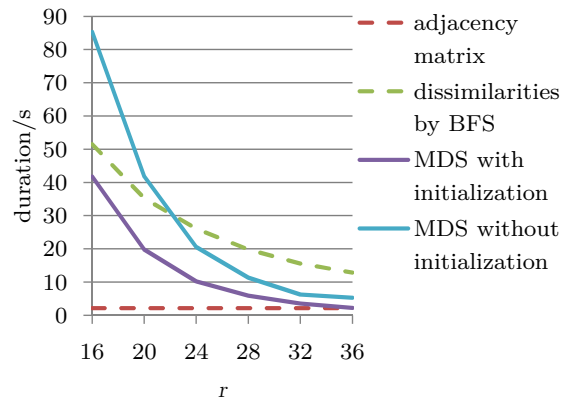
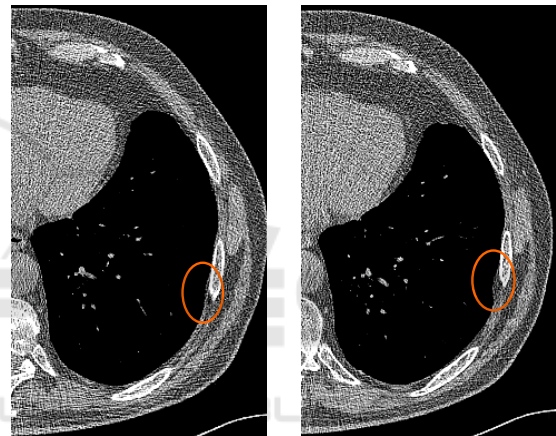
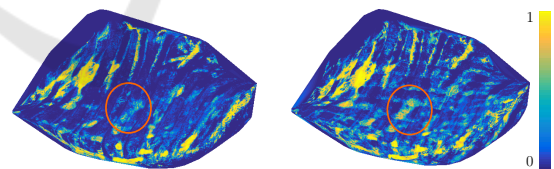


Figure 10: Computation time for the different parts of the algorithm, depending on the non-maxima suppression radius  $r$ .



(a) Slice view at point in time  $t_1$ .

(b) Slice view at point in time  $t_2$ .



(c) Planar representation of thickening probability at point in time  $t_1$ .

(d) Planar representation of thickening probability at point in time  $t_2$ .

Figure 11: Exemplary comparison of grown thickening (indicated by orange circle) between two points in time  $t_1$  and  $t_2$  utilizing the result of a pleura classification.

weight  $\kappa$  to reach a similar solution at both points in time. The stable stress values for increasing connection strength  $\kappa$ , shown in Figure 9a, indicate that temporal consistency has only a minor influence on the individual flattening quality. The suggested method results in planar representations of both points in time which are much better comparable then before, with minimal influence on the individual flattening. In

cases of  $\kappa > 0$ , the stress slightly increases with increasing radius  $r$  and at the same time, the temporal distance is decreasing. An increasing radius  $r$  results in a reduced number of constraints and therefore a less accurate but more consistent flattening at both points in time.

In the visualization of the non-aligned ( $\kappa = 0$ ) surfaces in Figure 8b, a rotation between the rib structures is visible whereas the aligned ( $\kappa = 500$ ) visualization reveals only minor differences between the surfaces. The different alignment for the non-connected MDS is mainly caused by the rotational DOF. An exemplary comparison of a single thickening at two points in time is shown in Figure 11.

The initialization with the prototype reduces the calculation time for the MDS approximately by a factor of 2, as shown by the blue and purple curve in Figure 10. For larger radii, the duration to calculate the dissimilarities by BFS is getting more dominant. The calculation of the adjacency matrix is independent of the chosen radius and therefore its computation time is constant.

## 5 CONCLUSIONS AND OUTLOOK

The presented approach results in a planar visualization of the lung surface, which enables a global assessment of the pleura. Potential findings can be exactly located and assessed regarding their extent. With the newly introduced temporal link, which improves the consistency of the visualizations from different points in time, the planar representation can also be utilized for a follow-up assessment. An important result is that this consistency does not have a considerable negative influence on the flattening quality. Additionally, with a closed-form initialization by a prototype lung, the MDS can be sped up. The new visualization can present simple scalar features. For a correct judgment of pleural thickenings, the 3D view is still required. However, the one-to-one mapping of 2D points and 3D points enables a synchronized 3D volume and planar visualization. With this synchronization, the user can benefit from both visualization types, as motivated in Figure 11. For documentation purposes, the planar representation itself is highly useful to record the final decision of the physician about the thickening locations.

Because of the rigid registration, only a rough mapping of surface points to the prototype is possible. This limits the use of the prototype lung to the initialization. With the presented approach, a permanent link of all prototype points during optimization,

similar to the temporal link, would have a negative impact on the flattening quality. However, a permanent link without negative influence on the flattening is desirable for inter-patient consistency and might be an interesting topic for future research.

## REFERENCES

- Bentley, J. L. (1975). Multidimensional binary search trees used for associative searching. *Commun. ACM*, 18(9):509–517.
- Bronstein, A. M., Bronstein, M. M., and Kimmel, R. (2003). Expression-invariant 3D face recognition. In *Audio-and Video-Based Biometric Person Authentication*, pages 62–70. Springer.
- Buja, A., Swayne, D. F., Littman, M. L., Dean, N., Hofmann, H., and Chen, L. (2008). Data visualization with multidimensional scaling. *Journal of Computational and Graphical Statistics*, 17(2):444–472.
- Carr, J. C., Fright, W. R., and Beatson, R. K. (1997). Surface interpolation with radial basis functions for medical imaging. *IEEE Transactions on Medical Imaging*, 16(1):96–107.
- Chen, M., Helm, E., Joshi, N., and Brady, M. (2011). Random walk-based automated segmentation for the prognosis of malignant pleural mesothelioma. In *IEEE International Symposium on Biomedical Imaging: From Nano to Macro*, pages 1978–1981. IEEE.
- Cox, T. F. and Cox, M. A. A. (2001). *Multidimensional Scaling*. CRC Press.
- Faltin, P., Chaisaowong, K., Ochsmann, E., and Kraus, T. (2013). Vollautomatische Detektion und Verlaufskontrolle der pleuralen Verdickungen. In 53. *Wissenschaftliche Jahrestagung der Deutschen Gesellschaft für Arbeitsmedizin und Umweltmedizin e.V. (DGAUM), Arbeitsmedizin in Europa, Muskel-Skelett-Erkrankungen und Beruf*, page 144, Bregenz (Austria).
- Floater, M. S. and Hormann, K. (2005). Surface parameterization: a tutorial and survey. In *Advances in multiresolution for geometric modelling*, pages 157–186. Springer.
- Frauenfelder, T., Tutic, M., Weder, W., Götti, R., Stahel, R., Seifert, B., and Opitz, I. (2011). Volumetry: an alternative to assess therapy response for malignant pleural mesothelioma? *European Respiratory Journal*, 38(1):162–168.
- Gleich, D. F. (2009). *Models and Algorithms for PageRank Sensitivity*. PhD thesis, Stanford University. Chapter 7 on MatlabBGL.
- Glocker, B., Komodakis, N., Paragios, N., and Navab, N. (2010). Non-rigid registration using discrete mrfs: Application to thoracic ct images. In *Workshop Evaluation of Methods for Pulmonary Image Registration, MICCAI 2010*.
- Grossmann, R., Kiryati, N., and Kimmel, R. (2002). Computational surface flattening: a voxel-based approach.

- IEEE Transactions on Pattern Analysis and Machine Intelligence*, 24(4):433–441.
- Hurdal, M. K. and Stephenson, K. (2009). Discrete conformal methods for cortical brain flattening. *Neuroimage*, 45(1):S86–S98.
- Kengne Nzegne, P., Faltin, P., Kraus, T., and Chaisaowong, K. (2013). 3D lung surface analysis towards segmentation of pleural thickenings. In *Bildverarbeitung für die Medizin 2013*, pages 253–258. Springer.
- Kruskal, J. B. (1964). Multidimensional scaling by optimizing goodness of fit to a nonmetric hypothesis. *Psychometrika*, 29(1):1–27.
- Morse, B. S., Yoo, T. S., Rheingans, P., Chen, D. T., and Subramanian, K. R. (2005). Interpolating implicit surfaces from scattered surface data using compactly supported radial basis functions. In *Proc. ACM SIGGRAPH*, pages 78–87. ACM.
- Navon, I. and Legler, D. M. (1987). Conjugate-gradient methods for large-scale minimization in meteorology. *Monthly Weather Review*, 115(8):1479–1502.
- Neubeck, A. and Gool, L. J. V. (2006). Efficient non-maximum suppression. In *Proc. of International Conference on Pattern Recognition*, pages 850–855.
- Ochsmann, E., Carl, T., Brand, P., Raithel, H., and Kraus, T. (2010). Inter-reader variability in chest radiography and HRCT for the early detection of asbestos-related lung and pleural abnormalities in a cohort of 636 asbestos-exposed subjects. *INTARCH OCC ENV HEA*, 83:39–46.
- Pistolesi, M. and Rusthoven, J. (2004). Malignant pleural mesothelioma: Update, current management, and newer therapeutic strategies. *Chest*, 126(4):1318–1329.
- Rudrapatna, M., Mai, V., Sowmya, A., and Wilson, P. (2005). Knowledge-driven automated detection of pleural plaques and thickening in high resolution CT of the lung. In *Information Processing in Medical Imaging*, pages 147–167. Springer.
- Rueckert, D., Sonoda, L. I., Hayes, C., Hill, D. L. G., Leach, M. O., and Hawkes, D. J. (1999). Nonrigid registration using free-form deformations: Application to breast MR images. *IEEE Transactions on Medical Imaging*, 18:712–721.
- Saroul, L., Figueiredo, O., and Hersch, R. D. (2006). Distance preserving flattening of surface sections. *IEEE Transactions on Visualization and Computer Graphics*, 12(1):26–35.
- Sensakovic, W. F., Armato III, S. G., Straus, C., Roberts, R. Y., Caligiuri, P., Starkey, A., and Kindler, H. L. (2011). Computerized segmentation and measurement of malignant pleural mesothelioma. *Medical physics*, 38(1):238–244.
- Tosun, D., Rettmann, M. E., and Prince, J. L. (2004). Mapping techniques for aligning sulci across multiple brains. *Medical image analysis*, 8(3):295–309.
- Virta, R. L. (2012). *2012 Minerals Yearbook*. U.S. Department of the Interior, U.S. Geological Survey.
- Zhao, X., Su, Z., Gu, X. D., Kaufman, A., Sun, J., Gao, J., and Luo, F. (2013). Area-preservation mapping using optimal mass transport. *Visualization and Computer Graphics, IEEE Transactions on*, 19(12):2838–2847.
- Zigelman, G., Kimmel, R., and Kiryati, N. (2002). Texture mapping using surface flattening via multidimensional scaling. *Visualization and Computer Graphics, IEEE Transactions on*, 8(2):198–207.